Fabrication of Highly-Aligned, Conductive, and Strong Graphene Papers Using Ultralarge Graphene Oxide Sheets

Xiuyi Lin,[†,§] Xi Shen,[†,§] Qingbin Zheng,[†] Nariman Yousefi,[†] Lin Ye,[‡] Yiu-Wing Mai,[‡] and Jang-Kyo Kim[†,*]

[†]Department of Mechanical Engineering, The Hong Kong University of Science and Technology, Clear Water Bay, Kowloon, Hong Kong and
[‡]Centre for Advanced Materials Technology, School of Aerospace, Mechanical and Mechatronic Engineering, The University of Sydney, Sydney, NSW 2006, Australia.
[§]Xiuyi Lin and Xi Shen share equal first authorship.

ABSTRACT This study demonstrates that large-size graphene oxide (GO) sheets can impart a tremendous positive impact on self-alignment, electrical conductivity, and mechanical properties of graphene papers. There is a remarkable, more than 3-fold improvement in electrical conductivity of the papers made from ultralarge GO sheets (with an average area of 272.2 μm^2) compared to that of the small GO counterpart (with an average area of 1.1 μm^2). The corresponding improvements in Young's modulus and tensile strength are equally notable, namely 320% and 280%, respectively. These improvements of bulk properties due to the large GO sheets are correlated to multiscale elemental and structural characteristics of GO sheets, such as the content of carboxyl groups on the GO edge, C/O ratio and Raman D/G-band intensity ratio of GO on the molecular-scale, and the degree of dispersion and stacking behavior of GO sheets on the microscale. The graphene papers made from larger GO sheets exhibit a closer-stacked structure and better alignment as confirmed by the fast Fourier transform analysis, to the benefits of their electrical conductivity and mechanical properties. The molecular dynamics simulation further elucidates that the enhanced intersheet interactions between large GO sheets play a key role in improving the Young's modulus of GO papers. The implication is that the said properties can be further improved by enhancing the intersheet stress transfer and electrical conduction especially through the thickness direction.

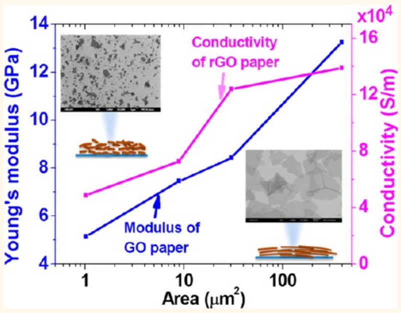

KEYWORDS: ultralarge graphene · GO paper · alignment · electrical conductivity · tensile properties · molecular dynamics simulation

Two-dimensional graphene and graphene-based materials have attracted tremendous interest from various research communities and much attention has been drawn to explore and apply their exceptional characteristics and properties.[1,2] Among several well-known techniques to synthesize graphene and its derivatives, the chemical method based on an earlier work[3] is the most popular and practical to obtain graphene oxide (GO) in an aqueous dispersion. GO consists of monolayer to several-layer graphene sheets with oxygenated functional groups on their basal plane and edges, and can be reassembled into thin films or paper-like materials in a freestanding form. GO papers are easily fabricated by stacking GO sheets *via* flow-directed assembly of aqueous GO dispersion.

This new material outperformed other paper-like materials in terms of mechanical properties,[4] while their tensile modulus and strength were comparable to those of flexible graphite foils and carbon nanotube bucky papers produced by filtration.[5] By mechanically compressing and thermally annealing the GO papers, an 80% increase and a 10% reduction in in-plane and through-the-thickness thermal conductivities, respectively, were achieved.[6] The combination of the exceptional mechanical properties,[7] thermal stability,[8] high electrical conductivity[9] and biocompatibility[10] make graphene papers a promising candidate for many technological applications, for example, ranging from free-standing flexible electrodes for Li-ion batteries and supercapacitors[11,12] to biomedical applications, such as inclusion in heart valves[10] and drug delivery,[13,14] transparent conducting films,[15−17] and nanocomposites.[18−20]

The lateral dimensions of precursor GO sheets may play an important role in

* Address correspondence to mejkkim@ust.hk.

Received for review August 26, 2012 and accepted November 21, 2012.

10.1021/nn303904z

determining the properties and applications of GO papers. Large area GO sheets are ideally suited in a number of applications, for example, 3D graphene-based networks in self-assembled hydrogels,[21] formation of nematic liquid crystals in an aqueous solution,[22] 2D aligned structure in polymer-based composites,[20] and conductive thin films for optoelectronic devices.[17] The larger GO sheets can give rise to a higher electrical conductivity of thin films due to the expected lower intersheet contact resistance than smaller ones.[23] However, there are a number of unresolved issues on how and to what extent the large area GO can improve the conductivity and other important characteristics. Obviously, a more systematic study is necessary to establish the GO size−property relationship and understand the mechanisms responsible for the findings. It is equally important to control the GO size when preparing the aqueous GO dispersion for specific end applications. Few papers have hitherto appeared in the open literature regarding the control of GO size in aqueous dispersion, including (i) chemical exfoliation by controlling the degree of oxidation and exfoliation procedure;[22,24,25] (ii) electrochemical technique by controlling the electrical current and reduction time under a constant potential;[26] (iii) oxidation path and mechanical energy, such as shaking and sonication;[27] and (iv) adjusting the pH value of GO dispersion followed by selective sedimentation.[28]

In this report, we present an efficient method to prepare highly aligned, conductive, and strong graphene papers using ultralarge monolayer GO sheets. We demonstrate that the precursor GO sheet size has substantial influences on the bulk properties of graphene papers, including the modulus, strength, electrical conductivity, and the degree of alignment of GO sheets. We identify several important characteristics of GO sheets which control the properties of graphene papers, namely the type and degree of oxygenation, carbon/oxygen ratio, Raman D/G-band peak intensity ratio and the degree of alignment of GO sheets. The fast Fourier transform analysis is used to evaluate the degree of GO sheet alignment, and the molecular dynamics simulations (MDS) reveal the dominant mechanism behind improved Young's modulus with larger GO size.

RESULTS AND DISCUSSION

Effects of GO Size on Chemistry and Structure of GO Sheets. Figure 1 presents the size distributions of four different groups of sorted GO sheets and the corresponding scanning electron microscope (SEM) images. The two-parameter Weibull model[29] was adopted for the evaluation of the area and perimeter distributions of GO sheets, and the relevant Weibull parameters are shown in Table 1. The Weibull moduli for different GO sheets were invariably close to unity, indicating very large data scattering due to the presence of many tiny GO sheets in all the size groups, which could not be eliminated using the current sorting method. Nevertheless, there was a substantial increment in area, almost an order of magnitude difference in mean area (and the standard deviation) between the individual groups, when the group was changed from small GO (S-GO) to large GO (L-GO), very large GO (VL-GO) and ultralarge GO (UL-GO) (see Table 1). The perimeter data also had a functionally similar variation in mean value to the GO area data.

It is worth noting that the surface chemistry of GO sheets was significantly influenced by the GO size. The X-ray photoelectron spectroscopy (XPS) spectra are presented in Figure 2a, and the corresponding carbon assignations are summarized in Table 2. The binding energies of the C−C and C−H bonds are assigned at 284.7 and 285.5 eV, respectively, whereas the peaks at 286.7, 287.6, and 289.2 eV are assigned to −C−OH, −C═O, and −COOH functional groups, respectively. Owing to the large chemical shift into the range of the −C═O emission, the C−O−C group is assigned with −C═O at 287.6 eV.[30] The larger the GO area was, the higher was the C/O ratio (Figure 2b), suggesting that the smaller GO contained relatively more oxygenated groups for a given GO surface area. The C/O atomic ratio is an important parameter for evaluating the degree of oxidation of GO sheets.[25] Among several different oxygenated groups, the relative percentage of −COOH groups consistently declined with increasing GO area (Table 2), or increased with increasing periphery/area ratio (Figure 2c). According to the Lerf-Klinowski model[31] (see Figure 2d), the carboxylic acids are present at the edges, whereas the hydroxyl and epoxide groups exist on the basal planes of GO sheets. As smaller GO sheets have a longer perimeter or edge length for a given area, i.e., a higher perimeter/area ratio (Table 1), the smaller GO sheets tend to contain more carboxyl groups, and *vice versa* for the hydroxyl and epoxide groups (Table 2).

The G-band in Raman spectroscopy is active in sp^2-hybridized carbon-based materials, while the D-band is activated when the defects participate in the double resonance Raman scattering near the K point of the Brillouin zone. Thus, the D- to G-band peak intensity ratios, I_D/I_G, are often used to indicate defects in the structure.[32] In Figure 2 panels e and f, I_D/I_G continued to decrease with increasing GO area, which is attributed to gradually fewer defects caused by edge boundaries on the larger GO sheets.[33] The minor down-shift of the G-band peak from 1954 to 1952 cm^{-1} when the GO size increased from S-GO to UL-GO further confirmed fewer defects in the graphitic structure of the larger area GO sheets.[34]

Effects of GO Size on Dispersion and Stacking Behavior of GO Sheets. The 2θ values corresponding to the X-ray diffraction (XRD) peaks of GO papers presented a rising trend with increasing GO sheet area, as shown in

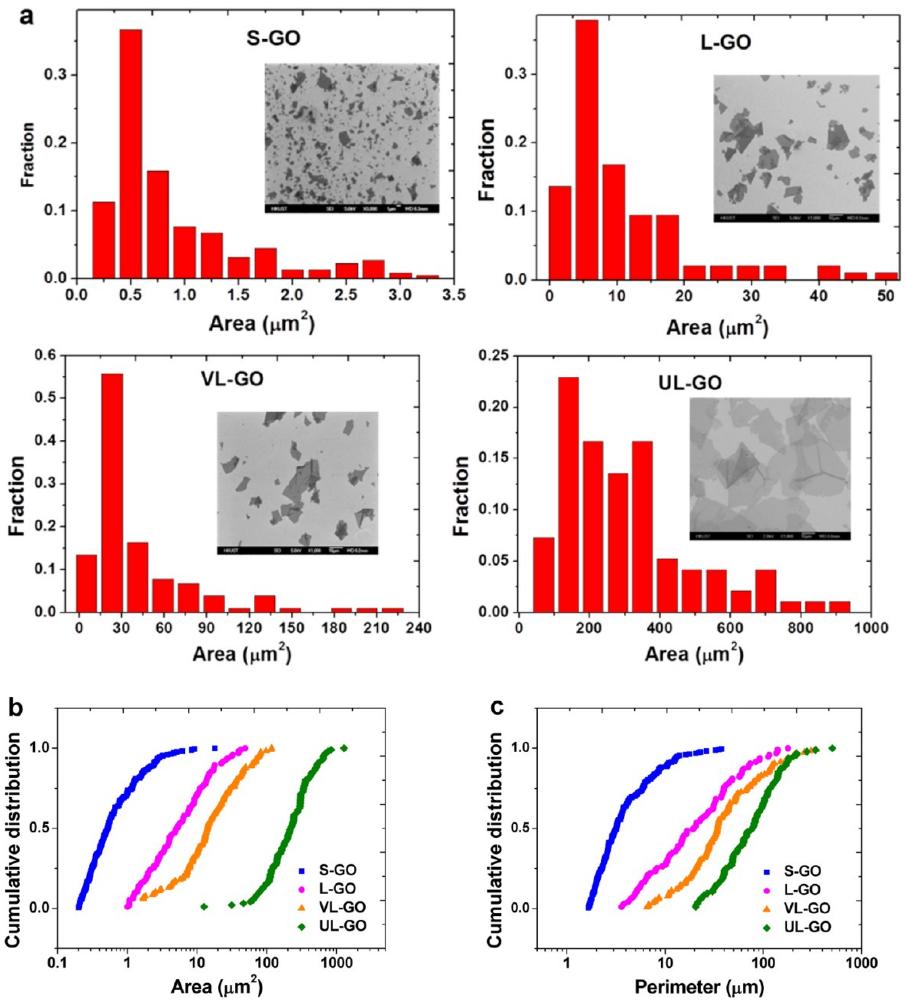

Figure 1. (a) Area distributions of GO sheets of different size groups S-GO, L-GO, VL- GO, and UL-GO (insets, typical SEM images used for measurements); Weibull plots of (b) area and (c) perimeter distributions of GO sheets.

TABLE 1. Weibull Parameters Determined from Area and Perimeter Distributions of GO Sheets

GO sheet	Weibull modulus, α	scale parameter, β (μm^2)	area (μm^2) (mean ± std)	perimeter (μm) (mean ± std)	perimeter/area ratio
S-GO	1.22	1.02	1.07 ± 1.7	5.4 ± 7.1	5.05
L-GO	1.13	8.9	9 ± 9.96	32.6 ± 35.1	3.62
VL-GO	1.09	30.37	32.2 ± 40.3	59.7 ± 68.8	1.85
UL-GO	1.39	394.9	272.2 ± 205.3	92.8 ± 72.7	0.34

Figure 3a. Conversely, the corresponding *d*-spacing between the adjacent GO sheets showed a falling trend, namely 9.52, 9.42, 9.14, and 8.58 Å for S-GO, L-GO, VL-GO, and UL-GO papers, respectively. These values are two to three times greater than the *d*-spacing of natural graphite, 3.35 Å.[35] The correlation between GO size and *d*-spacing is quite consistent with the previous report that the interlayer spacing in GO sheets was proportional to the degree of oxidation.[22,36] These findings have significant implications on the measured physical and mechanical properties, especially the electrical conductivity, modulus, and strength, by altering the compactness and cross-sectional area of the papers prepared from the same weight of precursor GO sheets. The different interlayer distances between GO sheets of different size groups can be explained by differing degrees of functionalization. The S-GO sheets with more oxygenated functional groups can absorb more water through hydrogen bonding during film formation under vacuum, inevitably increasing the interlayer distance to accommodate the water molecules. This statement is further supported by the moisture contents within the GO papers, which were measured to be 18.1%, 17.5%, 16.2%, and 15.8% for S-GO, L-GO, VL-GO, and UL-GO papers, respectively (see Supporting Information, Figure S4a). The enlarged interlayer distance on the subnanometer scale cannot be completely recovered

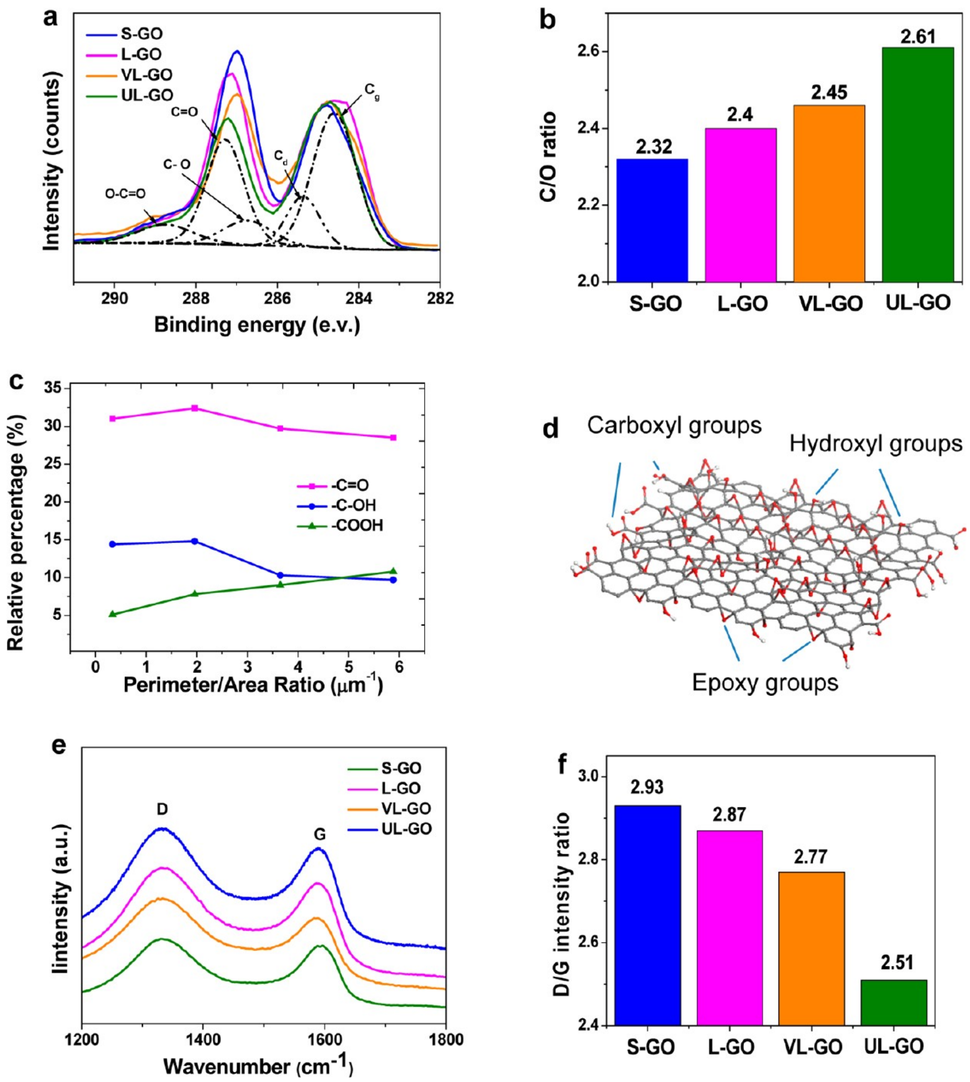

Figure 2. (a) XPS C1s spectra with carbon assignments; (b) corresponding carbon to oxygen ratio; (c) relative atomic contents of oxygenated functional groups; (d) schematic of molecular structures of GO; (e) Raman spectra D- and G-band peaks; and (f) the corresponding intensity ratios, I_D/I_G, for GO sheets of four different size groups.

TABLE 2. Relative Percentages of Carbon and Assignations of Four Different Sizes of GO Sheets

binding energy and assignation	Cg sp^2 ~284.7 eV	Cd sp^3 ~285.5 eV	−C−OH ~286.7 eV	−C=O ~287.6 eV	−COOH ~290.2 eV
S-GO	38.9	12.1	9.7	28.5	10.8
L-GO	39.6	11.4	10.3	29.7	9.0
VL-GO	36.7	8.3	14.8	32.4	7.8
UL-GO	36.8	12.7	14.4	31.0	5.1

to the inherent *d*-spacing of graphite even after oven drying.[37]

The surface charges of four groups of GO dispersions were characterized using a zeta potentiometer (Zeta Plus, BIC) and the results are summarized in Figure 3b. The zeta potential measures the electrostatic potential near the surface of suspended particles, which is related to the stability of colloidal dispersions because agglomeration of particles is avoided by electrostatic repulsion. The higher the zeta potential is, the higher is the stability of dispersion, and the dispersion can be regarded as microscopically stable when the absolute value of the zeta potential is above approximately 25 mV.[38] The zeta potential for S-GO was a remarkable −50.2 mV, which is attributed to a large number of oxygenated functional groups both at the edges and basal planes, causing strong repulsive force between the GO sheets in water. The absolute value decreased with increasing GO size (to −31.9 mV for UL-GO), due to the stronger attraction among the larger basal planes. A strong correlation between zeta potential and C/O ratio has been reported for

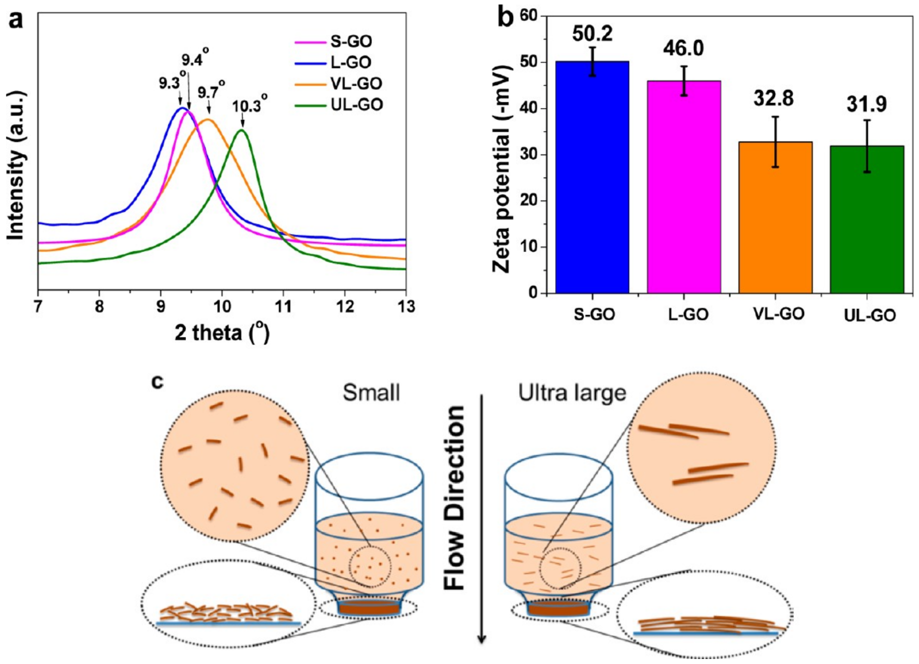

Figure 3. (a) XRD patterns and (b) zeta potentials of four different groups of GO papers; (c) schematic of self-assembly process during vacuum filtration of GO sheets of different sizes.

functionalized carbon nanotubes in different solvents.[38] It appears that the degree of attraction or repulsion between the GO sheets remained operational during the formation of the papers, allowing the larger area GO sheets to more tightly stack together to form better alignment.

In view of the properties of GO papers and the above discussion, the self-assembly process of GO papers is schematically presented (Figure 3c). Under the vacuum pressure, well-aligned GO papers are formed by accumulating individual sheets from bottom to top. There is a significant analogy between the GO sheets during paper formation in this study and the self-alignment of GO or rGO sheets in an aqueous polymer.[20] The GO sheets at a high concentration tended to self-adjust their basal plane perpendicular to the film thickness direction, resulting in significant alignment in the polymer matrix. The self-alignment appeared to be driven by several mechanisms, including the gravitational force in low viscous media,[39] steric hindrance between them, and the "excluded volume" interactions among the GO sheets of extremely large aspect ratios.[40] Other important mechanisms are the $\pi-\pi$ interaction and the van der Waals forces acting between the adjacent amphiphilic GO sheets consisting of both hydrophilic edges due to ionizable carbonyl/carboxyl groups and hydrophobic basal planes with isolated epoxy/hydroxyl groups.[20] However, it is not clear whether the larger GO sheets had stronger interactions or higher molecular forces to attract each other, leading to better alignment, than the smaller GO sheets.

Major parameters that make the stacking behavior different between the GO sheets of different sizes are the aspect ratio and the degree of functionalization. The higher the aspect ratio, the better is the alignment through the "excluded volume" interactions, as suggested by the formation of liquid crystals in UL-GO aqueous dispersion at a critical concentration of about 0.1 wt % GO or above.[22] It is already proven that the smaller GO sheets tended to have more carboxyl functional groups with a lower C/O ratio (Figure 2b,c), which in turn made the alignment of smaller GO sheets more difficult.

Effects of GO Size on Mechanical Properties and Electrical Conductivity of GO Papers. There were drastic enhancements in Young's modulus of GO papers with increasing GO size for both papers with and without water, as shown in Figure 4a,b. The improvements in Young's modulus of the UL-GO papers were remarkable with consistently more than 100% of the values measured for the S-GO papers. The improvement in tensile strength of GO papers with water was also equally remarkable, more than 100% from S-GO to UL-GO papers. A few reasons are thought to be responsible for these findings. First, the papers made from larger GO sheets tended to have a more compact and aligned structure than those with smaller sheets. As proven by the XRD and XPS analyses, the larger GO sheets with less oxygenated functional groups could absorb less water through hydrogen bonding, which in turn led to a smaller interlayer distance, giving rise to a smaller cross-sectional area with a denser structure for a given graphene weight content. The degree of alignment of GO papers was quantitatively evaluated based on the fast Fourier transform (FFT) method, which is discussed in the next section. Second, fewer defects

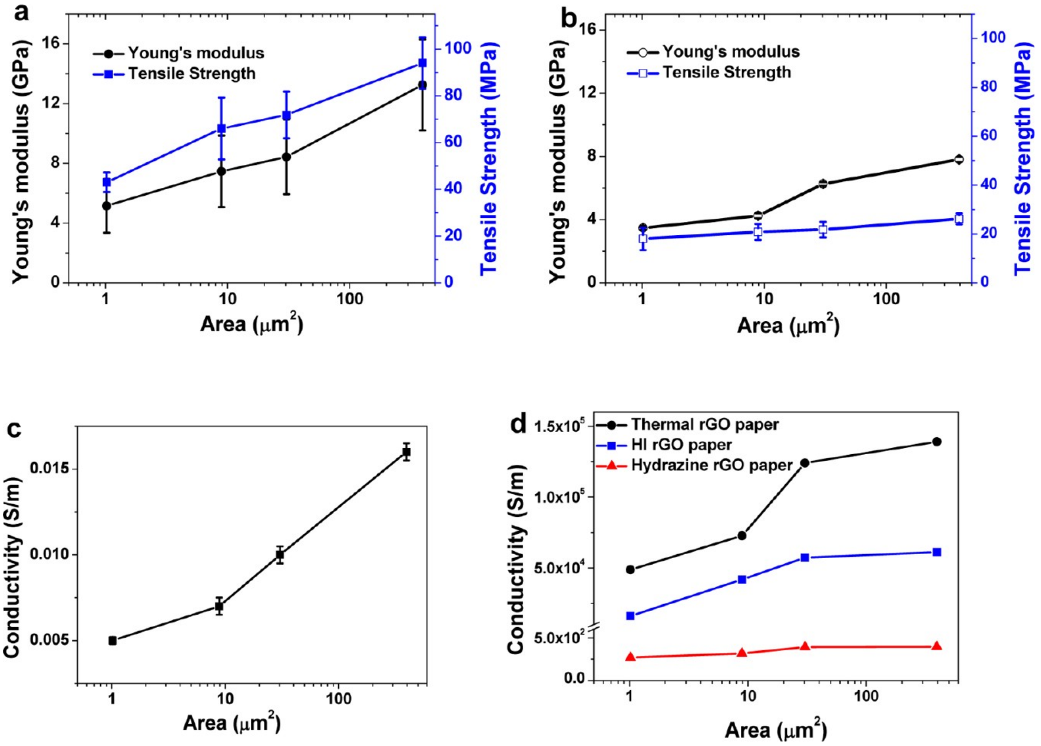

Figure 4. Changes in mechanical properties of GO papers (a) with and (b) without water measured as a function of average GO area; electrical conductivities of GO papers as a function of GO area (c) before and (d) after reduction.

or oxygenated functional groups were present in the larger GO sheets, which were also confirmed by the lower I_D/I_G intensity ratio. Third, another important reason is associated with the deformation mechanisms that are different depending on the GO size. Dominant mechanisms were identified through the MDS, which is discussed in the following. It is also worth mentioning that the modulus of GO papers with water was about twice higher than the corresponding values measured for papers without water, for all the GO sizes studied. This observation is expected and similar to the previous observation[36] because the removal of moisture eliminated the hydrogen bonds between GO sheets at the same time, leading to the diminution of interlayer cross-linking. The electrical conductivity of GO papers presented a functionally similar, consistent rise with an increase in the average GO size (Figure 4c). Basically the same trend with a more significant increment was noted after the reduction of GO papers (Figure 4d): for example, there were 185% and 283% improvements in conductivity for the thermally reduced and hydrogen iodine acid (HI)-reduced GO papers, respectively, with respect to GO average size change from S-GO to UL-GO. One of the major mechanisms behind this finding is the higher intersheet contact resistance[23,25] in the papers containing smaller GO sheets. It should be noted that the GO edges are known to have a high concentration of carboxyl functional groups which are highly insulating.[41,42] The higher degrees of compactness and alignment of the papers containing larger GO sheets may have also contributed to the increasing trend of electrical conductivity.

When the mechanical properties and electrical conductivities measured here were compared with those reported in the literature, there were mixed findings. The measured elastic moduli were similar to or only slightly higher than the reported values, whereas the electrical conductivity was significantly better than the literature values, see Supporting Information, Table S1. The moisture content and the hydrogen bonds between the GO sheets are the two most important factors controlling the elastic modulus of GO papers,[36] which appear to be more sensitive than the GO size studied here. Most of the GO papers used in the previous studies were either dried or tested at elevated temperatures to achieve low moisture content. As compared with GO papers with a similar moisture content, the UL-GO papers in this study exhibited generally higher modulus and strength. The much higher electrical conductivity obtained in this study arose from the combination of two synergistic effects, namely, the ultralarge size GO sheets and the effective reduction through high temperature annealing.

Alignment of GO Sheets in GO Papers. To support the above observations on mechanical and electrical properties as well as our claim on alignment, we developed a methodology to quantitatively measure the degree of alignment of the GO papers based on the fast Fourier transform (FFT) method.[43−46] In FFT, the complex spatial patterns represented by gray values in each

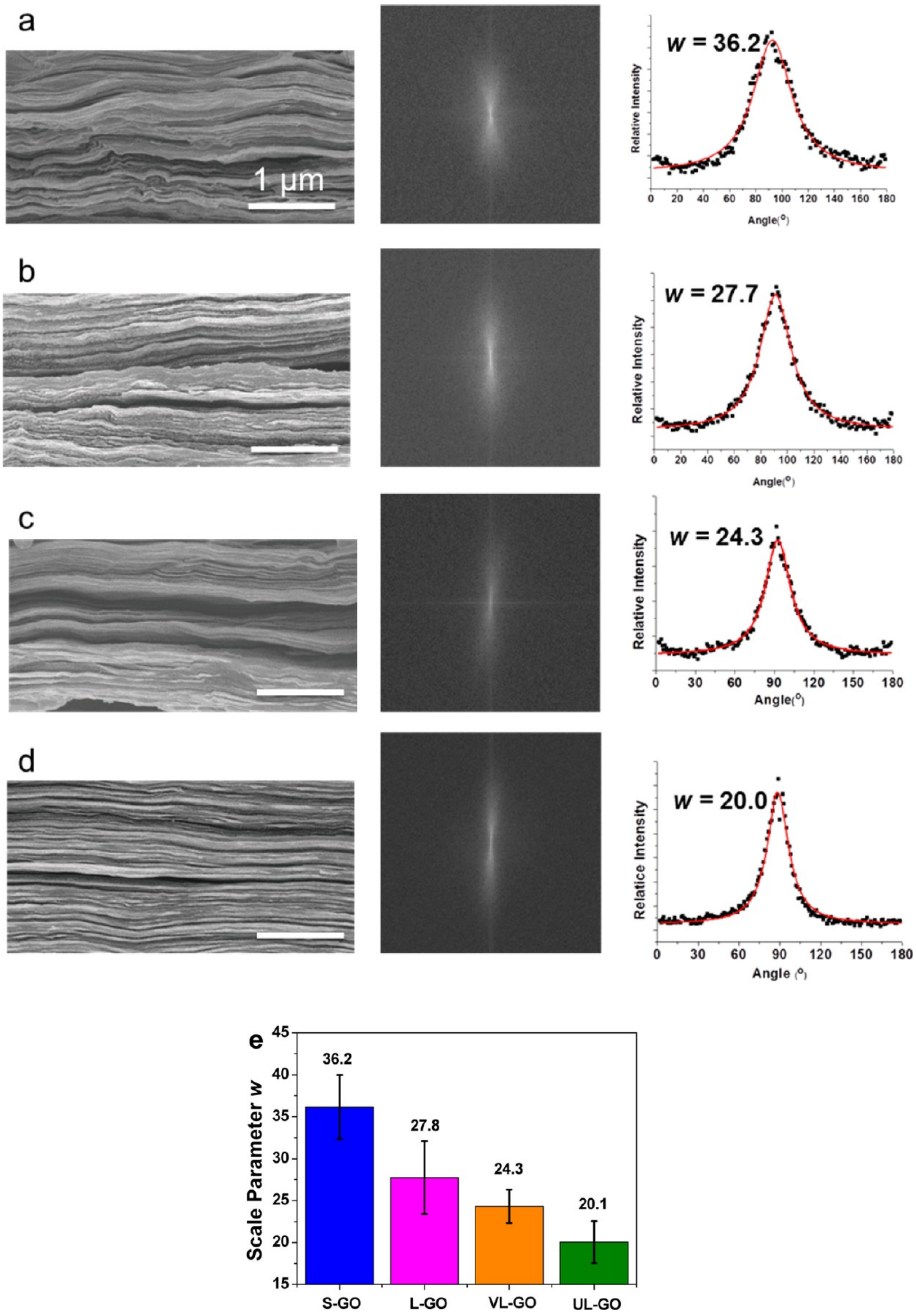

Figure 5. SEM images (left) of 2 μm × 4 μm cross-sectional area of GO papers, FFT frequency domain images (middle), and angular analysis fitted with the Cauchy–Lorentz distribution (right) for (a) S-GO (b) L-GO (c) VL-GO and (d) UL-GO papers; (e) scale parameters, *w*.

pixel $I[m,n]$ of an image is converted into direction-dependent frequency components, $F[u,v]$. Using a module in ImageJ, FFT is performed on each SEM image consisting of an area 2 μm × 4 μm, where the special image is converted to a frequency domain according to

$$F[u,v] = \frac{1}{MN}\sum_{m=0}^{M-1}\sum_{n=0}^{N-1} I[m,n]\exp\left(-i2\pi\left(\frac{um}{M}+\frac{vn}{N}\right)\right) \tag{1}$$

As an inherent property of the FFT frequency domain images, the intensity of each pixel presents an angular dependence on patterns of spatial alignment where pixels displaying high intensity values are clustered along the orientation of the highest degree of directional anisotropy. Thus, the FFT method is commonly used for analyzing the orientation properties of collagen bundles[43,44] and carbon-fiber reinforced composite.[45,46] For FFT images of GO papers, the angular distribution of

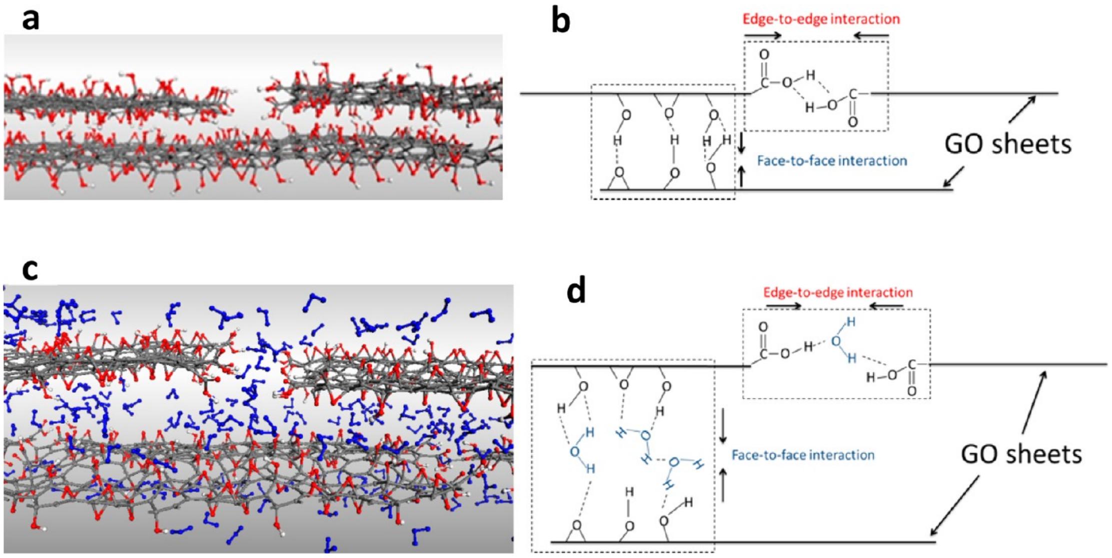

Figure 6. 3D model snapshots of GO sheets (a) without water and (c) with intercalated water molecules; and 2D schematics of GO paper models with functional groups bonded between adjacent GO sheets through hydrogen bonds (b) directly and (d) mediated by water molecules. Dash lines represent hydrogen bonds. The interaction energy was calculated in the rectangular area.

the intensity in the frequency domain images of GO papers demonstrated a good fit using the Cauchy–Lorentz distributions.

$$y = y_0 + \frac{2A}{\pi}\left(\frac{w}{4(x - x_0)^2 + w^2}\right) \qquad (2)$$

The location parameter, x_0, of the distribution represents the angle corresponding to the peak of the curve, about 90° as the principle orientation of the paper alignment, because the GO sheets are horizontally aligned. The scale parameter, w, specifies the half-width at half-maximum (HWHM) or half the line's peak value, presenting the angle of deviation from the principle orientation and thus measures the degree of alignment. Figure 5 presents SEM images of GO paper cross sections, the FFT frequency domain images, and the corresponding results of angular analysis. There was a linear decrease in the w value with increasing GO size, clearly indicating that the larger the GO sheet area was, the better was the alignment of the GO papers (Figure 5e). For information, the image with perfectly aligned parallel layers has a w value of 3.4.

Mechanisms of Improved Young's Modulus of GO Papers with Large GO Sheets. To understand the mechanisms behind the aforementioned mechanical properties, MDS were carried out using the program, Materials Studio (Accerlrys). GO paper models were built consisting of two sheets of monolayer GO containing oxygenated functional groups according to the Lerf–Klinowski model[31] (Figures 2d and 6). Moisture was also taken into account by randomly adding water molecules to the models, while the content was kept constant at 16 wt % to avoid the complications arising from its effect.[36,47] The energy-strain curves and the Young's moduli for the GO papers with differing sizes are shown in Figure 7a,b. The Young's moduli for the GO papers both with and without water increase consistently as the GO sheet size increases by about five times from 1.1 to 5.4 nm. For the models containing the same size GO sheets, the GO papers with water always show higher Young's moduli than their counterparts without water. The results were extrapolated using a logarithmic fitting equation, as shown in Figure 7c, to estimate the dependence of Young's modulus on GO size on the micrometer scale, as seen in practical GO papers. The comparison between the extrapolated curve and the experimental data (see Figure 4a,b) indicates that while the MD simulation correctly predicted the general trend, the predictions were approximately an order of magnitude higher than the experimental results. Such a large discrepancy is expected and can be attributed to the idealized, defect-free models used in the simulation, whereas the GO paper samples used in experiments always contained crumpled and folded GO sheets with defects induced during the oxidation process. Misalignments between the GO sheets in the experimental GO papers have also contributed significantly to the discrepancy. These structural flaws substantially reduced the load transfer efficiency between adjacent GO sheets as well as the inherent stiffness of individual GO.

A further probe was made into the exact deformation mechanisms between the GO sheets to gain insight into the improved Young's modulus of the papers with larger GO sheets. There are two components of deformation which contribute to the total tensile deformation of GO papers: namely, (i) GO sheets deformation, that is, elongation of GO sheets themselves as a result of stretching, bending, and torsion of carbon–carbon bonds within the GO sheets; and

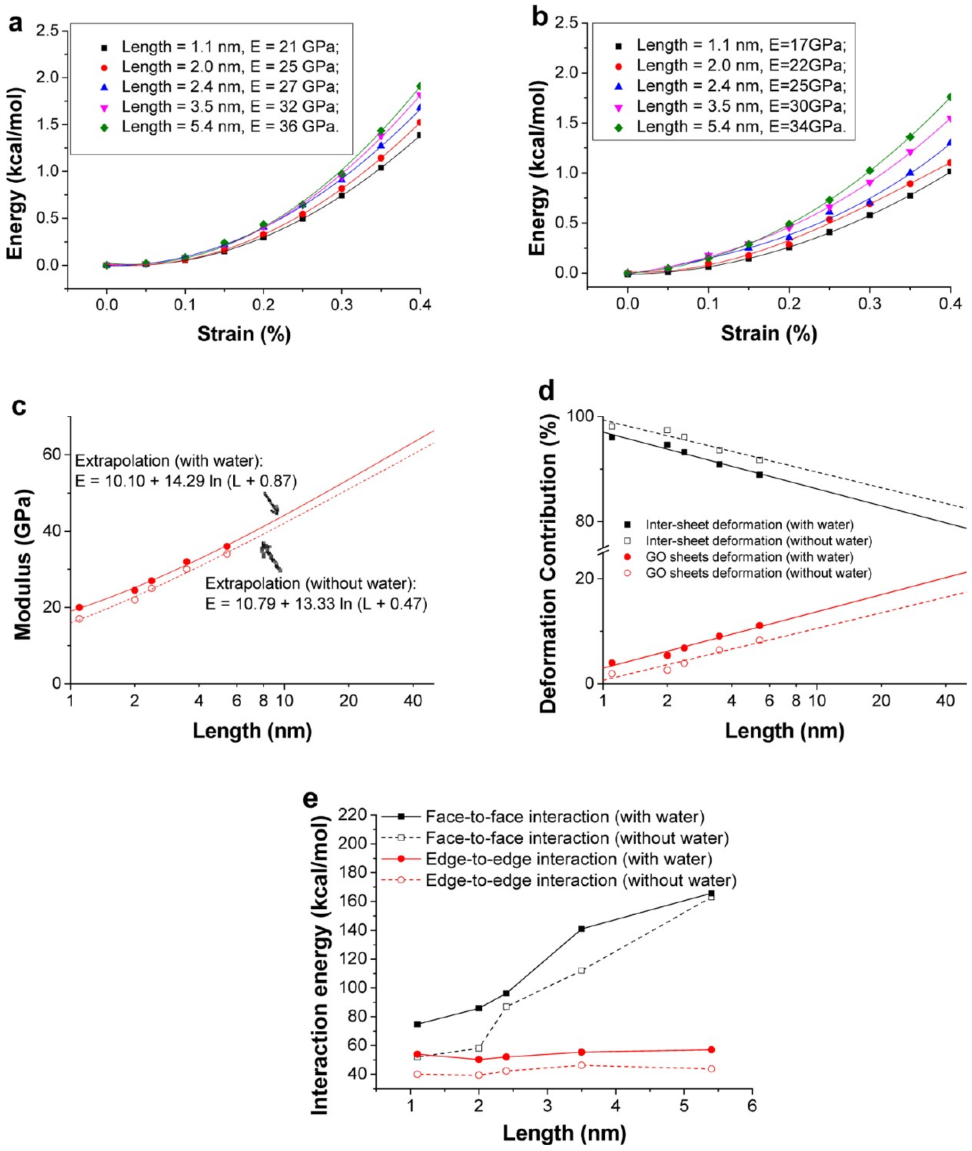

Figure 7. Energy–strain curves of GO papers with different GO size groups (a) with and (b) without water; (c) extrapolation of modulus values; (d) plots of two different components of deformation as a function of GO length. Solid and dash lines are linear extrapolations of the data; and (e) face-to-face and edge-to-edge interaction energies as a function of GO length.

(ii) intersheet deformation taking place in the form of relative displacement between the GO sheets in the same as well as in the different horizontal plane(s) causing stretching of hydrogen bonds formed between the functional groups in tension and shear. The contributions of the two different components to the total deformation of GO papers are plotted as a function of GO size in Figure 7d. More than 90% of the deformation is predicted to originate from the intersheet deformation regardless of the GO size on the nanoscale. The extrapolation also indicates that the contribution from the deformation of GO sheets increases linearly as the GO size increases, reaching almost 20% of the total when the average GO size is above 50 nm. This observation practically implies that the tensile deformation of GO papers is dominated by the intersheet deformation while the elongation of the GO sheets becomes gradually more important as the GO size increases.

Since the intersheet deformation is the major component of deformation in GO papers, the next question is why the papers made from larger size GO can resist intersheet deformation more efficiently to yield a higher Young's modulus. The intersheet deformation was hindered by the interactions between adjacent sheets both in the same and different horizontal planes through hydrogen bonds. As shown in Figures 6b,d, we define the interaction between adjacent GO sheets in the same horizontal plane as *edge-to-edge interaction* while that in different horizontal planes as *face-to-face interaction*. Although the edge-to-edge interaction energy remained almost the same low value, the face-to-face interaction energy increased due to the increasing contact area (Figure 7e). Because the face-to-face interaction energy was increasingly higher than the edge-to-edge interaction energy when the GO size increased, the former energy dominated in impeding the intersheet deformation of GO papers. The increasing face-to-face interaction energy directly translates into increasing interactions between adjacent GO sheets, discouraging the intersheet deformation and consequently rising Young's modulus.

Meanwhile, as the minor contribution, the deformation of GO sheets became increasingly important with increasing GO size. GO sheet deformation caused stretching of the carbon—carbon covalent bonds within the GO sheets, requiring more energy than simply stretching the weak intersheet hydrogen bonds like in intersheet deformation. Because the contribution of GO sheet deformation continuously increased with GO size, more energy was required to deform GO papers and consequently a higher Young's modulus was expected.

Similar predictions of tensile strengths are also possible if proper failure criteria are established. Summarizing the above findings, the Young's modulus of GO papers both with and without water increased with increasing GO size, confirming the experimental finding, although there were large differences in absolute value between experiment and prediction owing to the presence of numerous flaws and GO sheet misalignments in the experimental GO papers. The Young's modulus was controlled predominantly by the shear deformation taking place between the monolayer GO sheets and its influence became less dominant with increasing GO size. While the stretching of GO sheets themselves in tension had a negligible positive effect on the Young's modulus of GO papers with GO size on a nanoscale, it became increasingly important when the GO size was on a microscale as in practical GO papers.

CONCLUSION

We report a simple and effective method to sort as-prepared GO sheets into several groups of uniform sizes based on a centrifugation method. The surface chemistry, structural morphology, dispersion characteristics and degree of alignment of GO papers were shown to depend largely on the precursor GO sheet size. The GO papers made of larger GO sheets were proven to possess significantly higher mechanical properties and electrical conductivity than those with smaller sheets. The former papers had a more densely stacked structure, fewer defects as evidenced by the higher C/O ratio and lower D/G intensity ratio, and better alignment. MDS revealed the dominant mechanisms underlying the improvement of Young's modulus by increasing the GO size. Larger GO sheets resulted in enhanced interaction energy between adjacent GO sheets in different planes which in turn hindered the shear deformation of the GO papers. The contribution from the tensile elongation of the GO sheets became increasingly important with increasing GO size. The above findings have practical implications that these properties can be improved by enhancing the intersheet transfer of stress and electrical conduction, for example, *via* chemical cross-linking.[4,9,48]

METHODS

Preparation of Sorted GO Dispersion. The precursor GO dispersion was synthesized based on the well-established chemical method[3,49] using natural graphite flakes, and the detailed procedure is presented in the Supporting Information. The as-prepared GO dispersion with polydispersity was sorted into four different groups of uniform sizes via three-step centrifugation (Supporting Information, Figure S2). The GO dispersion was initially centrifuged at 8000 rpm for 40 min on a table-top centrifuge (SIGMA 2-16P), dividing into supernatant and precipitate. The precipitate was collected for the second round of centrifugation; while the supernatant was labeled as small GO (S-GO). The collected precipitate was dispersed in water again and centrifuged at 6000 rpm for 40 min, producing supernatant and precipitate, the latter being labeled as large GO (L-GO). The precipitate was dispersed in water again for the third round of centrifugation at 4000 rpm for 40 min. The produced supernatant was marked as very large GO (VL-GO) and the precipitate as ultralarge GO (UL-GO). The sorted GO sheets had mean areas of 1.1, 9.0, 32.2, and 272.2 μm^2, respectively, for S-GO, L-GO, VL-GO and UL-GO. To measure the size of GO sheets, the sorted GO dispersion was diluted using methanol in the ratio of 1:50, and its droplets were applied on the silicon wafer and dried to take clear images of GO under SEM. The software ImageJ was employed to analyze a total of more than 100 GO sheets for each condition. The scale was set according to the magnification of SEM images, then the original SEM images were converted into binary images, followed by defining the GO sheet edges, and finally the average area and perimeter were calculated using the software, see Supporting Information, Figure S2.

Preparation of GO and Reduced GO Papers. GO papers were prepared by filtration of GO dispersions of four different size groups before or after reduction through the membrane filter (Anodisc, 47 mm in diameter, 0.2 μm in pore size, supplied by Whatman) under vacuum pressure. The thickness of GO papers was varied between 1 and 10 μm depending on the type of experiment by controlling the amount of GO or reduced GO (rGO) dispersion. After filtration, the paper was peeled off from the filter and dried in an oven at 60 °C for 7 days. Before the tensile tests and electrical conductivity measurements, all the papers were stored in a container with desiccant to maintain a constant moisture content of $16 \pm 2\%$. GO papers without water were prepared by drying in an oven at 150 °C for 72 h to remove the water molecules entrapped between the GO sheets.[50] Three different methods were chosen to reduce the GO at different stages of fabrication, including (i) reduction of GO sheets using hydrazine, (ii) reduction of GO papers by immersing in hydrogen iodine (HI) solution, and (iii) reduction of GO papers through high temperature treatment. See Supporting Information, Figure S3 for further details.

Characterization. The tapping-mode atomic force microscope (AFM, Digital Instruments) was employed to evaluate the morphology and thickness of GO sheets. The images taken from the SEM were processed using the software ImageJ to analyze the area and perimeter of GO sheets. X-ray photoelectron spectroscopy (XPS, Axis Ultra DLD) was used to characterize the elemental compositions and the assignments of the carbon peaks of GO papers before and after reduction. Raman spectroscopy (Renishaw MicroRaman/Photoluminescence System) was used to analyze the carbon structure of as-produced and reduced GO sheets using a 633 nm He−Ne laser. The interlayer distance between adjacent GO layers was measured on an X-ray diffraction system (XRD, X'pert Pro, PANalytical) using Cu Kα1 (λ = 0.154 nm) radiation. Zeta potentials of the GO dispersions were measured using an analyzer (Brookhaven ZetaPlus) at room temperature. The electrical conductivity was measured using the four probe method (Scientific Equipment & Services) where the GO papers were coated with silver at the contact points to reduce the contact resistance. The mechanical properties of GO papers were measured on a dynamic mechanic analyzer (Perkin-Elmer) at room temperature; 20 mm x 3 mm rectangular samples were loaded in tension with a preload of 50 mN and at a controlled ramp rate of 50 mN/min.

Molecular Dynamics Simulations. Two sets of GO paper models both with and without water were built using monolayer GO sheets with periodic boundary conditions implemented along the short direction (*y*-axis) and out-of-plane direction (*z*-axis), and with a 100-Å-thick vacuum slab along the loading direction (*x*-axis) to prevent any interaction between the periodic images. The boundary carbon atoms at the right edge were fixed, and a displacement ΔL was applied to the carbon atoms at the left edge. For each set, five models with the same number of carbon atoms and different GO lengths were constructed (see Supporting Information and Figure S5 for more details). Three epoxy groups and one hydroxyl group per 12 carbon atoms were randomly distributed along both sides of graphene basal plane. Five carboxyl groups per edge were attached to the GO sheet edges, resulting in a higher density of carboxyl groups in the model with smaller GO sheets. These models yielded C/O ratios ranging from 2.17 for the smallest size to 2.68 for the largest size, in line with the compositions of our experimental samples (Figure 2b,c). The Young's modulus of the GO papers was determined by fitting the energy-strain curves:[51]

$$E = \frac{1}{V}\frac{\partial^2 U}{\partial \varepsilon^2} \qquad (3)$$

where the potential energy, U, corresponding to each strain, ε, was obtained by varying the displacement, ΔL. V is the unit volume of the model. The COMPASS (condensed-phase optimized molecular potentials for atomistic simulation studies) force field[52] was used to simulate interatomic interactions. As the first *ab initio*-based force field to be parametrized using extensive data for molecules in the condensed phase, the COMPASS force field has been shown to provide accurate properties of many materials.[52−54] All the simulations were carried out in the canonical ensemble where the total number of atoms N and the volume V remained constant with a time step of 1 fs. The temperature was maintained at 1 K using Andersen thermostat. The pressure control was achieved by the Berendsen barostat. The group-based cutoff distance for nonbond interactions was 9.5 Å. Energy minimization was performed using a conjugate-gradient algorithm implemented in Materials Studio succeeding each dynamics run to ensure that the total potential energy of the system reached the minimum.

Conflict of Interest: The authors declare no competing financial interest.

Acknowledgment. This project was financially supported by the Research Grants Council of Hong Kong SAR through the General Research Funds (Project Codes 614010 and 613811). X.L. was partly supported by the Postgraduate Scholarship through the Nano Technology Program at HKUST, and X.S. was a recipient of a Hong Kong Ph.D. Fellowship Award. Part of the paper was presented at the 15th European Conference on Composites Materials (Venice, Italy in June 2012), and X.L. was awarded the Best Poster Award (1st Prize).

Supporting Information Available: Three different methods used to reduce the GO or GO papers at different stages of fabrication; SEM images used to measure the area and perimeter of GO sheets; and the configurations of molecular dynamics simulation models used to predict the Young's modulus of GO papers. This material is available free of charge *via* the Internet at http://pubs.acs.org.

REFERENCES AND NOTES

1. Geim, A. K. Graphene Status and Prospects. *Science* **2009**, *324*, 1530–1534.
2. Geim, A. K.; Novoselov, K. S. The Rise of Graphene. *Nat. Mater.* **2007**, *6*, 183–191.
3. Hummers, W. S., Jr.; Offeman, R. E. Preparation of Graphitic Oxide. *J. Am. Chem. Soc.* **1958**, *80*, 1339.
4. Park, S.; Lee, K. S.; Bozoklu, G.; Cai, W.; Nguyen, S. B. T.; Ruoff, R. S. Graphene Oxide Papers Modified by Divalent Ions—Enhancing Mechanical Properties *via* Chemical Cross-Linking. *ACS Nano* **2008**, *2*, 572–578.
5. Dikin, D. A.; Stankovich, S.; Zimney, E. J.; Piner, R. D.; Dommett, G. H. B.; Evmenenko, G.; Nguyen, S. T.; Ruoff, R. S. Preparation and Characterization of Graphene Oxide Paper. *Nature* **2007**, *448*, 457–460.
6. Xiang, J.; Drzal, L. T. Thermal Conductivity of Exfoliated Graphite Nanoplatelet Paper. *Carbon* **2011**, *49*, 773–778.
7. Ranjbartoreh, A. R.; Wang, B.; Shen, X.; Wang, G. Advanced Mechanical Properties of Graphene Paper. *J. Appl. Phys.* **2011**, *109*, 014306.
8. Barnard, A. S.; Snook, I. K. Thermal Stability of Graphene Edge Structure and Graphene Nanoflakes. *J. Chem. Phys.* **2008**, *128*, 09470.
9. Compton, O. C.; Dikin, D. A.; Putz, K. W.; Brinson, L. C.; Nguyen, S. T. Electrically Conductive "Alkylated" Graphene Paper *via* Chemical Reduction of Amine-Functionalized Graphene Oxide Paper. *Adv. Mater.* **2010**, *22*, 892–896.
10. Chen, H.; Müller, M. B.; Gilmore, K. J.; Wallace, G. G.; Li, D. Mechanically Strong, Electrically Conductive, and Biocompatible Graphene Paper. *Adv. Mater.* **2008**, *20*, 3557–3561.
11. Huang, Z. D.; Zhang, B.; Zheng, Q. B.; Oh, S. W.; Lin, X. Y.; Yousefi, N.; Kim, J. K. Self-Assembled Reduced Graphene Oxide/Carbon Nanotube Thin Films as Electrodes for Supercapacitors. *J. Mater. Chem.* **2012**, *49*, 3591–3599.
12. Zhang, B.; Zheng, Q. B.; Huang, Z. D.; Oh, S. W.; Kim, J. K. SnO_2−Graphene−Carbon Nanotube Mixture for Anode Material with Improved Rate Capacities. *Carbon* **2011**, *13*, 4524–4534.
13. Sun, X.; Liu, Z. Welsher, K.; Robinson, J.; Goodwin, A.; Zaric, S.; Dai, H. Nano-graphene Oxide for Cellular Imaging and Drug Delivery. *Nano Res.* **2008**, *1*, 203–212.
14. Liu, Z.; Robinson, J. T.; Sun, X.; Dai, H. PEGylated Nanographene Oxide for Delivery of Water-Insoluble Cancer Drugs. *J. Am. Chem. Soc.* **2008**, *130*, 10876–10877.
15. Becerril, H. A.; Mao, J.; Liu, Z.; Stoltenberg, R. M.; Bao, Z.; Chen, Y. Evaluation of Solution-Processed Reduced Graphene Oxide Films as Transparent Conductors. *ACS Nano* **2008**, *2*, 463–470.
16. Wang, S. J.; Geng, Y.; Zheng, Q. B.; Kim, J. K. Fabrication of Highly Conducting and Transparent Graphene Films. *Carbon* **2010**, *48*, 1815–1823.
17. Zheng, Q. B.; Ip, W. H.; Lin, X. Y.; Yousefi, N.; Yeung, K. K.; Li, Z. G.; Kim, J. K. Transparent Conductive Films Consisting of Ultralarge Graphene Sheets Produced by Langmuir−Blodgett Assembly. *ACS Nano* **2011**, *5*, 6039–6051.
18. Kim, H. W.; Abdala, A. A.; Makosco, C. W. Graphene/Polymer Nanocomposites. *Macromolecules* **2010**, *43*, 6515–6530.
19. Potts, J. R.; Dreyer, D. R.; Bielawski, C. W.; Ruoff, R. S. Graphene-Based Polymer Nanocomposites. *Polymer* **2011**, *52*, 5–25.
20. Yousefi, N.; Gudarzi, M. M.; Zheng, Q. B.; Aboutalebi, S. H.; Sharif, F.; Kim, J. K. Self-Alignment and High Electrical Conductivity of Ultralarge Graphene Oxide−Polyurethane Nanocomposites. *J. Mater. Chem.* **2012**, *22*, 12709–12717.
21. Xu, Y.; Sheng, K.; Li, C.; Shi, G. Self-Assembled Graphene Hydrogel *via* a One-Step Hydrothermal Process. *ACS Nano* **2010**, *4*, 4324–4330.
22. Aboutalebi, S. H.; Gudarzi, M. M; Zheng, Q. B.; Kim, J. K. Spontaneous Formation of Liquid Crystals in Ultralarge

Graphene Oxide Dispersions. *Adv. Funct. Mater.* **2011**, *15*, 2978–2988.

23. Li, C. Y.; Thostenson, E. T.; Chou, T. W. Dominant Role of Tunneling Resistance in the Electrical Conductivity of Carbon Nanotube-Based Composites. *Appl. Phys. Lett.* **2007**, *91*, 223114.
24. Zhang, L.; Liang, J.; Huang, Y.; Ma, Y.; Wang, Y.; Chen, Y. Size-Controlled Synthesis of Graphene Oxide Sheets on a Large Scale Using Chemical Exfoliation. *Carbon* **2009**, *47*, 3365–3368.
25. Zhao, J. P.; Pei, S. F.; Ren, W. C.; Gao, L. B. Efficient Preparation of Large-Area Graphene Oxide Sheets for Transparent Conductive Films. *ACS Nano* **2010**, *4*, 5245–5252.
26. Peng, X.; Liu, X.; Diamond, D.; Lau, K. T. Synthesis of Electrochemically-Reduced Graphene Oxide Film with Controllable Size and Thickness and Its Use in Supercapacitor. *Carbon* **2011**, *49*, 3488–3496.
27. Pan, S.; Aksay, I. A. Factors Controlling the Size of Graphene Oxide Sheets Produced *via* the Graphite Oxide Route. *ACS Nano* **2011**, *5*, 4073–4083.
28. Wang, X.; Bai, H.; Shi, G. Size Fractionation of Graphene Oxide Sheets by pH-Assisted Selective Sedimentation. *J. Am. Chem. Soc.* **2011**, *133*, 6338–6342.
29. Weibull, W. Stockholm, S. A Statistical Distribution Function of Wide Applicability. *J. Appl. Mech.* **1951**, *18*, 293–297.
30. Yang, D.; Velamakanni, A.; Bozoklu, G.; Park, S.; Stoller, M.; Piner, R. D.; Stankovich, S.; Jung, I.; Field, D. A.; Ventrice, C. A., Jr.; *et al.* Chemical Analysis of Graphene Oxide Films after Heat and Chemical Treatments by X-ray Photoelectron and Micro-Raman Spectroscopy. *Carbon* **2009**, *47*, 145–152.
31. Casabianca, L. B.; Shaibat, M. A.; Cai, W. W.; Park, S.; Piner, R.; Ruoff, R. S.; Ishii, Y. NMR-Based Structural Modeling of Graphite Oxide Using Multidimensional ^{13}C Solid-State NMR and *ab Initio* Chemical Shift Calculations. *J. Am. Chem. Soc.* **2010**, *132*, 5672–5676.
32. Pimenta, M. A.; Dresselhaus, G.; Dresselhaus, M. S.; Cançado, L. G.; Jorio, A.; Saito, R. Studying Disorder in Graphite-Based Systems by Raman Spectroscopy. *Phys. Chem. Chem. Phys.* **2007**, *9*, 1276–1291.
33. Su, C. Y.; Xu, Y.; Zhang, W.; Zhao, J.; Tang, X.; Tsai, C. H.; Li, L. J. Electrical and Spectroscopic Characterizations of Ultra-large Reduced Graphene Oxide Monolayers. *Chem. Mater.* **2009**, *21*, 5674–5680.
34. Dreyer, D. R.; Park, S. J.; Bielawski, C. W.; Ruoff, R. S. The Chemistry of Graphene Oxide. *Chem. Soc. Rev.* **2010**, *39*, 228–240.
35. McAllister, M. J.; Li, J.; Adamson, D. H.; Schniepp, H. C.; Abdala, A. A.; Liu, J.; Herrera-Alonso, M.; Milius, D. L.; Car, R.; Prud'homme, R. K.; *et al.* Single Sheet Functionalized Graphene by Oxidation and Thermal Expansion of Graphite. *Chem. Mater.* **2007**, *19*, 4396–4404.
36. Medhekar, N. V.; Ramasubramaniam, A.; Ruoff, R. S.; Shenoy, V. B. Hydrogen Bond Networks in Graphene Oxide Composite Paper: Structure and Mechanical Properties. *ACS Nano* **2010**, *4*, 2300–2306.
37. Hsiao, M. C.; Liao, S. H.; Yen, M. Y.; Teng, C. C.; Lee, S. H.; Pu, N. W.; Wang, C. A.; Sung, Y.; Ger, M. D.; Ma, C. C. M.; *et al.* Preparation and Properties of a Graphene Reinforced Nanocomposite Conducting Plate. *J. Mater. Chem.* **2010**, *20*, 8496–8505.
38. Ma, P. C.; Siddiqui, N. A.; Mäder, E.; Kim, J. K. Correlation between Electrokinetic Potential, Dispersibility and Surface Chemistry and Energy of Carbon Nanotubes. *Compos. Sci. Technol.* **2011**, *71*, 1644–1651.
39. Ansari, S.; Kelarakis, A.; Estevez, L.; Giannelis, E. P. Oriented Arrays of Graphene in a Polymer Matrix by *in Situ* Reduction of Graphite Oxide Nanosheets. *Small* **2010**, *6*, 205–209.
40. Lyatskaya, Y.; Balazs, A. Modeling the Phase Behavior of Polymer−Clay Composites. *Macromolecules* **1998**, *19*, 6676–6680.
41. Kim, J.; Cote, L. J.; Kim, F.; Yuan, W.; Shull, K. R.; Huang, J. X. Graphene Oxide Sheets at Interfaces. *J. Am. Chem. Soc.* **2010**, *132*, 8180–8186.
42. Erickson, K.; Erni, R.; Lee, Z.; Alem, N.; Gannett, W.; Zettl, A. Determination of the Local Chemical Structure of Graphene Oxide and Reduced Graphene Oxide. *Adv. Mater.* **2010**, *22*, 4467–4472.
43. Lu, K.; Chen, J.; Zhuo, S.; Zheng, L.; Jiang, X.; Zhu, X.; Zhao, J. Multiphoton Laser Scanning Microscopy of Localized Scleroderma. *Skin Res. Technol.* **2009**, *15*, 489–495.
44. Cicchi, R.; Kapsokalyvas, D.; De Giorgi, V.; Maio, V.; Van Wiechen, A.; Massi, D.; Lotti, T.; Pavone, F. S. Scoring of Collagen Organization in Healthy and Diseased Human Dermis by Multiphoton Microscopy. *J. Biophotonics* **2010**, *3*, 34–43.
45. Smith, R. A.; Nelson, L. J.; Mienczakowski, M. J.; Challis, R. E. Automated Analysis and Advanced Defect Characterisation from Ultrasonic Scans Of Composites. *Insight* **2009**, *1*, 82–87.
46. Nishimura, T.; Ansell, M. Fast Fourier Transform and Filtered Image Analyses of Fiber Orientation in OSB. *Wood Sci. Technol.* **2002**, *36*, 287–307.
47. Compton, O. C.; Cranford, S. W.; Putz, K. W.; An, Z.; Brinson, L. C.; Buehler, M. J.; Nguyen, S. T. Tuning the Mechanical Properties of Graphene Oxide Paper and Its Associated Polymer Nanocomposites by Controlling Cooperative Intersheet Hydrogen Bonding. *ACS Nano* **2012**, *6*, 2008–2019.
48. An, Z.; Compton, O. C.; Putz, K. W.; Brinson, L. C.; Nguyen, S. T. Bio-inspired Borate Cross-Linking in Ultra-stiff Graphene Oxide Thin Films. *Adv. Mater.* **2011**, *23*, 3842–3846.
49. Geng, Y.; Wang, S. J.; Kim, J. K. Preparation of Graphite Nanoplatelets and Graphene Sheets. *J. Colloid Interface Sci.* **2009**, *336*, 592–598.
50. Acik, M.; Mattevi, C.; Gong, C.; Lee, G.; Cho, K.; Chhowalla, M.; Chabal, Y. J. The Role of Intercalated Water in Multilayered Graphene Oxide. *ACS Nano* **2010**, *4*, 5861–8.
51. Zheng, Q. B.; Geng, Y.; Wang, S. J.; Li, Z. G.; Kim, J. K. Effects of Functional Groups on the Mechanical and Wrinkling Properties of Graphene Sheets. *Carbon* **2010**, *48*, 4315–4322.
52. Sun, H.; Ren, P.; Fried, J. R. The COMPASS Force Field: Parameterization and Validation for Polyphosphazenes. *Comput. Theor. Polym. Sci.* **1998**, *8*, 229–246.
53. Sun, H.; Rigby, D. Polysiloxanes: *Ab Initio* Force Field and Structural, Conformational and Thermophysical Properties. *Spectrosc. Acta, Part A* **1997**, *53*, 1301–1323.
54. Grujicic, M.; Cao, G.; Roy, W. N. Atomistic Modeling of Solubilization of Carbon Nanotubes by Non-covalent Functionalization with Poly(*p*-phenylenevinylene-co-2,5-dioctoxy-*m*-phenylenevinylene). *Appl. Surf. Sci.* **2004**, *227*, 349–363.